DOI: 10.15480/882.9327

Eighth International Symposium on Marine Propulsors
smp'24, Berlin, Germany, March 2024

Influence of the rheological properties of fluid mud on the open water diagram of the DTC propeller *

Ivan Shevchuk[1], **Moustafa Abdel-Maksoud**[1], **Nino Ohle**[2]

[1]Hamburg University of Technology
[2]Hamburg Port Authority

ABSTRACT

The paper presents the results of a CFD study regarding DTC propeller performance in fluid-mud. Since the fluid mud has non-Newtonian rheological properties, conventional CFD models used in the marine context are not applicable in this case and the development and validation of a new simulation environment is required. The development included the implementation of the new rheological model closely capturing the experimental stress-strain curve, multi-fluid solver (air/water/fluid-mud) and the novel turbulence modeling approach, applicable to the fluids with fluctuating apparent viscosity. The developed computational framework is validated in this work for the case of prediction of the resistance of a flat plate submerged into the fluid-mud. Afterwards, the series of open water tests is performed for the DTC propeller for different parameters of the fluid mud and different submersion depths. The fraction of fluid mud in the propeller disk, the limiting viscosity and the fluid mud density are varied in the systematic manner, as these are found to be of the highest significance. This way it is possible to assess the influence of these parameters on the open water diagram of the propeller. For example it is shown, that the fluid mud density is increasing the thrust and torque coefficients at the same time and thus the propeller efficiency remains almost the same. Based on the collected data the correlations are derived and an actuator disk model is developed, which takes into account the influence of particular fluid mud sample on the thrust and torque characteristics. Since the final aim of the project is to predict the maneuvering properties of ship moving in proximity (or in direct contact) of fluid mud, an adequate actuator disk model is required for efficient computations. Direct resolution of propeller geometry in maneuvering simulations is computationally inefficient.

Keywords Open water diagram, Multiphase, non-Newtonian fluid, actuator disk.

1 INTRODUCTION

The performance of the marine propeller in fluid mud (which is a non-Newtonian medium) is a topic which is almost absent from literature, because the propeller in reality never works under such conditions. However, at the same time due to two reasons the relevance of fluid mud influence on the ship hydrodynamics is rapidly increasing. First is the constant increase of ships' sizes, leading to the situation where the ships move with low under keel clearance (UKC). So there is a high possibility of the interaction with the fluid mud layers near the bottom. The second reason, specific to some ports (e.g. Hamburg), is that the amount of fluid mud accumulating annually in the port area is increasing over the last years. This in turn increases the dredging costs. One way to reduce the constant increase in costs is to quantify the possible alterations in maneuvering characteristics when the vessel is in contact with fluid mud, and then develop recommendations to ensure the safe performance of typical port maneuvers. In order to conduct a simulation of such maneuvers, the exhaustive numerical model of the multi-component fluid is required, including one (or multiple) non-Newtonian layers.

Simulation of the ship maneuvers with the geometrically resolved rotating propeller is a very expensive computational task. The time scales of propeller rotation are orders of magnitude smaller than that of the ship maneuver and therefore the computation would require a very small time step and would have to be conducted over very long time periods. In order to avoid such scenarios, the geometrical model of the propeller is usually replaced by the so-called actuator disk model, which imitates the integral effect of the propeller on the flow (axial flow acceleration, torque, resistance increase, etc.). Normally, actuator disk models use the open-water diagram of the particular propeller in order to replicate the correct response to the change of the wake fraction in the propeller plane. Such open water diagrams are created for the cases, where the propeller operates in water. However, in the maneuvers considered in the current research the propeller may be partly submerged into the fluid mud. In this scenario the open water diagram of the propeller may be significantly changed. To study the influence of fluid mud on the propeller open water diagram, the CFD investigation into this influence was performed in this work. The propeller rotation in contact with fluid mud with varied rheological properties was simulated.

2 MATHEMATICAL MODEL

The multiphase volume-of-fluid (VOF) solver is implemented in OpenFOAM. The system of equations for this case can be written as follows:

$$\frac{\partial \rho \overline{u}_i}{\partial t} + \frac{\partial (\rho \overline{u}_i \overline{u}_j)}{\partial x_j} = \tag{1}$$

$$- \frac{\partial \overline{p_d^*}}{\partial x_i} + \frac{\partial}{\partial x_j}\left[\mu_{tot}\left(\frac{\partial \overline{u}_i}{\partial x_j} + \frac{\partial \overline{u}_j}{\partial x_i}\right)\right] - g_i x_i \frac{\partial \rho}{\partial x_i} \tag{2}$$

$$\frac{\partial \overline{u}_i}{\partial x_i} = 0 \tag{3}$$

$$\frac{\partial \alpha_1}{\partial t} + \frac{\partial \alpha_1 \overline{u}_j}{\partial x_j} + \frac{\partial}{\partial x_j}(\alpha_1 \alpha_2 u_{r,j}) + \frac{\partial}{\partial x_j}(\alpha_1 \alpha_3 u_{r,j}) = 0 \tag{4}$$

$$\frac{\partial \alpha_2}{\partial t} + \frac{\partial \alpha_2 u_j}{\partial x_j} - \frac{\partial}{\partial x_j}(\alpha_2 \alpha_1 u_{r,j}) = 0 \tag{5}$$

$$\alpha_3 = 1 - \alpha_1 - \alpha_2 \tag{6}$$

$$\rho = \rho_1 \alpha_1 + \rho_2 \alpha_2 + \rho_3 \alpha_3 \tag{7}$$

$$\nu = \frac{\rho_1 \alpha_1 \nu_1 + \rho_2 \alpha_2 \nu_2 + \rho_3 \alpha_3 \nu_3}{\rho_1 \alpha_1 + \rho_2 \alpha_2 + \rho_3 \alpha_3} \tag{8}$$

where $\overline{\mathbf{u}}$ - Reynolds-averaged velocity vector ($\overline{u}_1, \overline{u}_2, \overline{u}_3$ - its components), $\overline{p_d^*} = \overline{p^*} - \rho g_j x_j$ - dynamic pressure, $\mu_{tot} = (\nu_t + \nu + C_\tau \mu_{nn})\rho$ is the total dynamic viscosity, $\mathbf{g}$ - gravitational acceleration, $\alpha_n \in [0; 1]$ - volume fraction of the n-th phase, ρ - density of the mixture, variable is space, ρ_n - density of the n-th phase, $\mathbf{u}_r$ - compression velocity, directed normal to the interface. It can be noticed that the compression velocity in the compression term of the equation for α_2 has a negative sign. The reason for that is the fact, that the compression term for α_2 has to have the opposite direction, as compared to that of α_1, whereas the compression velocity $\mathbf{u}_r$ is computed just once.

One can see, that the transport equation (4) contains an additional non-linear term $\frac{\partial}{\partial x_j}(\alpha_1 \alpha_2 u_{r,j})$, which is not present in the usual convection equation. This term is added for compression of the interface and is purely artificial.

Additionally, it has to be mentioned, that the kinematic viscosity ν_3 in the fluid mud region is the so-called apparent viscosity, varying in space and depending on the magnitude of the strain rate tensor S_{ij}, $\nu = F(\dot{\gamma}) = F(\sqrt{2 S_{ij} S_{ij}})$. The resulting kinematic viscosity of the mixture is defined according to eq. (8).

At the moment the solver was tested only for a system with three components (fluids): air, water and fluid mud, two of which can be mixed (water/fluid mud) but it can easily be extended to a larger number of components if a more complex model of a muddy bottom, containing multiple samples with different densities is required.

For the description of the rheological parameters of the fluid mud the six parameters model of Shakeel and Chassagne (Shakeel 2022) is used. It defines the shear stress as a combination of static and fluidic branches and therefore is able to capture the typical double-yield feature of the stress-strain curve:

$$\tau = \lambda \tau_{stat} + (1 - \lambda)\tau_{fluid} \tag{9}$$

$$\lambda = 1 - \frac{1}{1 + e^{-10(\dot{\gamma} - \dot{\gamma}_0)}} \tag{10}$$

$$\tau_{stat} = \frac{\tau_s}{1 + \frac{\dot{\gamma}_s}{\dot{\gamma}}} \tag{11}$$

$$\tau_{fluid} = \tau_s + \frac{\tau_f}{1 + \frac{\dot{\gamma}_f - \dot{\gamma}_0}{\dot{\gamma} - \dot{\gamma}_0}} + \mu_\infty(\dot{\gamma} - \dot{\gamma}_0). \tag{12}$$

The parameters of the model are τ_s, τ_f, $\dot{\gamma}_s$, $\dot{\gamma}_f$, $\dot{\gamma}_0$, μ_∞, which are determined by least-squares fitting of the experimental stress-strain curve of the particular sample. An example of the stress-strain curve is shown in Figure 1.

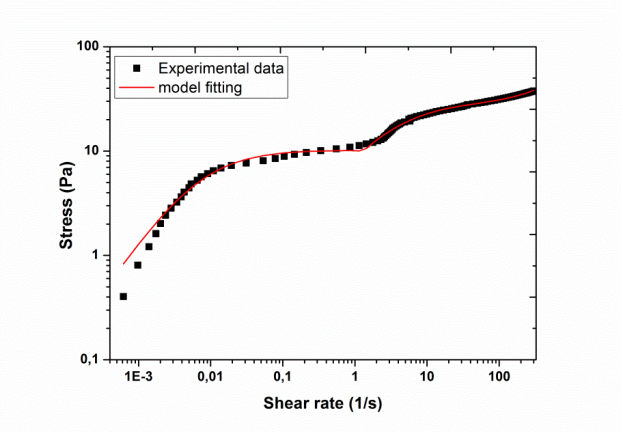

Figure 1: Example of the experimentally obtained stress-strain curve of the fluid mud and its fit by the Shakeel-Chassagne model

The apparent viscosity, used in the momentum equation is computed as:

$$\nu = \frac{\tau}{\dot{\gamma}} = \frac{\lambda \tau_{stat} + (1 - \lambda)\tau_{fluid}}{\dot{\gamma}}. \tag{13}$$

2.1 Turbulence modeling

During the well-known derivation of the RANS momentum equation, it is assumed that the viscosity ν is constant in time. In non-Newtonian fluids this assumption does not hold and therefore the averaging of the term $\frac{\partial}{\partial x_j}(2\mu S)$, which in the Newtonian fluids yields $\frac{\partial}{\partial x_j}(2\mu \overline{S})$, produces an additional term $\frac{\partial}{\partial x_j}(2\overline{\mu' S'_{ij}})$. To model this term Gavrilov and Rudyak (Gavrilov & Rudyak 2016) propose the formula, analogous to the Boussinesq hypothesis: $\frac{\partial}{\partial x_j}(2\overline{\mu' S'_{ij}}) \approx \frac{\partial}{\partial x_j}\left[2 C_\tau \mu_{nn} \overline{S}_{ij}\right]$. Together with the conventional eddy-viscosity model this yields:

$$\frac{D \rho \overline{u}_i}{Dt} = -\frac{\partial \overline{p}}{\partial x_i} + \frac{\partial}{\partial x_j}\left[2(\mu + \mu_t + C_\tau \mu_{nn})\overline{S}_{ij}\right], \tag{14}$$

where C_τ is a model parameter and μ_{nn} is the additional viscosity. The model proposed by Rudyak and Gavrilov determines μ_{nn} in terms of the parameters of the rheological model and the turbulence quantities used in four-equation

$\zeta - f$ model of (Hanjalic et al. 2004). Due to its complexity, it was decided to avoid the implementation of this model and use a simpler one proposed by (Lovato et al. 2022, 1), based on the $k - \omega$ SST model. There, the μ_{nn} reads:

$$\mu_{nn} = \frac{\partial \mu}{\partial \dot{\gamma}} \frac{\rho C_\beta \beta^* \omega k}{\mu \dot{\gamma}}. \tag{15}$$

where C_τ is a model parameter and μ_{nn} is the additional viscosity. The shear rate in this modeling approach includes the contribution from the modeled turbulence and is defined as:

$$\dot{\gamma}^2 = 2 S_{ij} S_{ij} + \frac{\rho C_\beta \beta^* \omega k}{\mu}. \tag{16}$$

The k and ω equations also have to be modified in order to account for the viscosity fluctuations:

$$\frac{Dk}{Dt} = \frac{\partial}{\partial x_j}\left[(\nu + \sigma_k \nu_t)\frac{\partial k}{\partial x_j}\right] + \widetilde{\mathcal{P}}_k - \beta^* k\omega + \xi_{nn} + \chi_{nn} \tag{17}$$

$$\frac{D\omega}{Dt} = \frac{\partial}{\partial x_j}\left[(\nu + \sigma_\omega \nu_t)\frac{\partial \omega}{\partial x_j}\right] + (1 - F_1) C D_{k\omega} + \frac{\alpha}{\nu_t}\widetilde{\mathcal{P}}_k - \beta\omega^2 + E_{nn}. \tag{18}$$

Here the terms $\xi_{nn}, \chi_{nn}, E_{nn}$ represent the work of non-Newtonian stresses, turbulent diffusion due to viscosity fluctuations and the non-Newtonian contribution to dissipation respectively (Gavrilov & Rudyak 2016). In the model of Lovato et al., these terms are given by the following formulas:

$$\chi_{nn} = -C_\chi \mu_{nn} S^2 \tag{19}$$

$$\xi_{nn} = C_\xi \nabla \cdot \left(\frac{\partial \mu}{\partial \dot{\gamma}} \frac{S^2}{\dot{\gamma}} \nabla k\right) \tag{20}$$

$$E_{nn} = C_E \frac{\rho \alpha}{\mu_t}(\xi_{nn} + \chi_{nn}) \tag{21}$$

For the complete set of model constants the reader is referred to the original paper. This model was implemented in OpenFOAM and was compared to the original implementation in ReFresco (by S. Lovato).

3 VALIDATION OF THE NUMERICAL MODEL

In order to validate the numerical model, the series of measurements of the resistance of a flat plate towed in fluid mud was conducted in the flume at Deltares. The experimental setup and the results are thoroughly described in the paper of (Lovato et al. 2022, 2), therefore only a brief description will be given in the present work.

Table 1: Particulars of the Deltares experiment

Plate	
Chord [m]	0.8
Thickness [m]	0.012
Submerged span [m]	0.96 or 1.0
Speed [m/s]	0.27,0.52,0.77,1.02
Flume	
Length [m]	30
Width [m]	2.4
Mud level [m]	1.96 or 2.0
Depth [m]	2.5

The flat plate was towed at four different speeds submerged into the fluid-mud. For the particulars, the reader is referred to Table 1. The measurements were carried out for three different fluid-mud samples. In order to reduce the amount of information presented in the paper, only the fluid-mud samples having τ_f of 10 and 17 Pa were tested.

The CFD simulations were conducted in order to reproduce the results of the Deltares tests and determine the level of accuracy of the CFD model applied in the current research. The computations were carried out for the mud samples Mud10 and Mud17 (named according to the yield stress of the sample) for the speeds of 0.27, 0.52, 0.77, 1.02 m/s. This yields in total 8 computations. An unstructured hex-dominant grid containing 6.8M cells was used in the simulations, which is depicted in Figure 2. The grid generation was performed using the `snappyHexMesh` tool from the OpenFOAM library. The deformation of the free surface was considered to be negligible and therefore the air/mud interface was modeled by a symmetry plane. The sharp edges of the plate were slightly rounded to improve mesh quality. The grid was not adapted for each towing speed because the y^+ value was 0.1 for the highest one and therefore was below 0.1 for all other speeds, which is considered sufficient. For all calculations the `simpleFoam` solver was used.

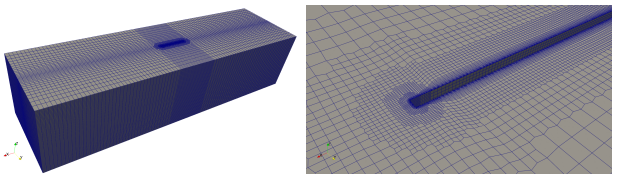

(a) (b)

Figure 2: Computational grid: a - overall structure, b - the mesh at the leading edge of the plate including the boundary layer grid

In Tables 2 and 3 the comparison between the numerical and experimental data is shown. At the lowest speed CFD overestimates the forces by about 13%. For higher speeds, the discrepancy first drops to about 1%, and then grows to 5-6% for the highest one, where CFD already underestimates the resistance. Similar trend is obtained by (Lovato et al. 2022, 2). In the cited paper it is discussed, that the possible source for the discrepancy is the fact that during

the experiment the plate could have had a non-zero angle of attack. By using the angle of attack of 3° the authors could improve the slope of the resistance curve. Such tests have not been conducted in the framework of this research, because the exact value of the angle of attack is unknown and therefore the results would be inconclusive anyway.

Table 2: Comparison of the CFD results with the experimental ones for the flat plate in fluid mud with $\tau_f = 10$ Pa

U [m/s]	F_{EXP} [N]	F_{CFD} [N]	E%D
0.27	17.70	20.04	13.23
0.52	20.41	21.69	6.26
0.77	23.73	23.83	0.44
1.02	27.74	26.40	-4.85

Table 3: Comparison of the CFD results with the experimental ones for the flat plate in fluid mud with $\tau_f = 17$ Pa

U [m/s]	F_{EXP} [N]	F_{CFD} [N]	E%D
0.27	30.40	34.24	12.64
0.52	34.46	36.44	5.77
0.77	38.60	39.05	1.17
1.02	45.13	42.31	-6.25

4 PROPELLER PARTICULARS AND CONDITIONS

The propeller to be studied in this work package is the DTC propeller (el Moctar et al., 2012), which is 5-bladed fixed pitch propeller with the right sense of rotation. The geometry used in the open water test and the surface mesh are shown in Figure 3, the model scale is considered. The propeller particulars can be seen in Table 4. For the considered scale, $n = 40$ was selected, whereas V_A was varied from 0.3 to 6 m/s.

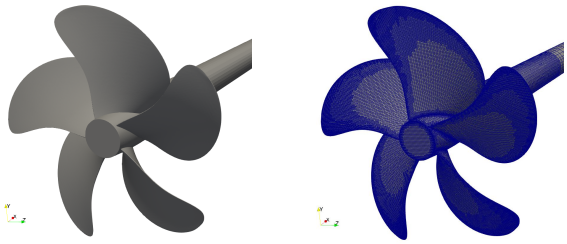

(a) (b)

Figure 3: The geometry of the DTC propeller and its surface mesh

Table 4: Particulars of the DTC propeller at model scale

D_p	[m]	0.15
$P_{0.7}/D_P$	[-]	0.959
A_e/A_0	[-]	0.8
$C_{0.7}$	[m]	0.054
θ	[°]	31.97
d_h/D_p	[-]	0.176
λ	[-]	59.4

5 SELECTION OF THE CORRELATION PARAMETERS

A large number of parameters can in theory influence the forces on the propeller and thus the open water characteristics. These are for example:

- fluid mud density
- rheological parameters of the fluid mud (τ_f, τ_s, γ_f, γ_s, μ_∞ etc.)
- fraction of fluid mud in propeller plane
- distance to the (hard) bottom
- distance to the free surface

Obviously, inclusion of all those parameters into the model would require enormous amount of computations and would produce a model with a high complexity, where the parameters could not be defined based on local flow quantities or parameters of the medium (e.g. density), but rather on some global parameters (distance to free surface, etc.). Therefore, it was decided, to pay attention only to the parameters which (in the spirit) of the CFD models can be defined in terms of local flow quantities or those describing the medium, i.e. the fraction of fluid mud in the propeller plane and its rheological properties.

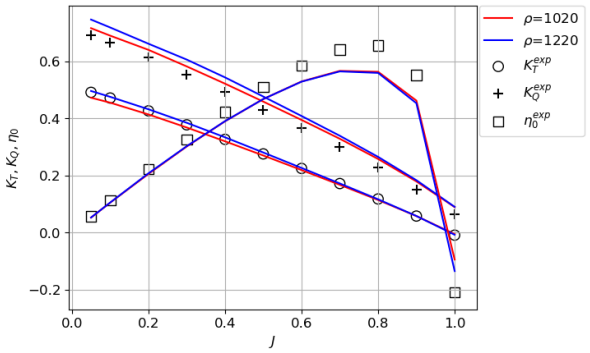

Figure 4: The open water diagram for the artificial mud samples with the same stress-strain curves, but different densities. The experimental data are shown for the conventional open water tests ($\rho = \approx 1000$).

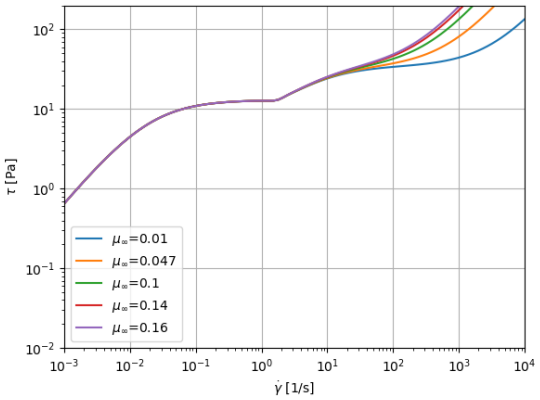

Figure 5: The stress-strain curves for different μ_∞

After a number of computational tests, it was revealed, that the density variation plays a very little role for the open water diagram. The computations were conducted for four artificial fluid mud samples, having the same stress-strain curve, but different densities. In Figure 4 the comparison of open water diagrams for the cases ρ_m = 1020 and ρ_m = 1220 is shown. It can be seen, that the increase of density by almost 20% yields only small change in the K_T and K_Q curves, which is moreover limited to small J. Therefore the density was considered to be of minor importance for the considered task.

Furthermore, the parameters of the stress-strain curve would play an important role in the case where the local linear velocity of the propeller blade would be small, for example at small r (distance from the propeller axis) or when the rps is small. Normally, for the propeller design conditions, the linear velocities of the points on the blades are very high and would lead to high values of the shear rate, meaning, that in this case only the parameter μ_∞ plays a significant role, whereas all effects of double yielding may be dismissed from consideration $\tau_s, \tau_f, \gamma_s, \gamma_f$.

As the result of presented reasoning, only two parameters were accounted for: the ratio $\frac{\mu_\infty}{\mu_w}$ and α, where μ_w is the dynamic viscosity of water and α is the fraction of fluid mud in the propeller plane.

6 DEPENDENCE ON THE VISCOSITY RATIO

In order to understand how the viscosity ratio influences the open water diagram, a series of the open water diagrams were generated for different fluid-mud samples based on the CFD computations.

Table 5: Fitting coefficients for the variation of the K_T and K_Q

	ΔK_T	ΔK_Q
a_1	0.0701	0.1296
a_2	-0.0026	-0.0717
a_3	-0.0015	0.0007
a_4	-0.1577	-0.2634
a_5	0.0010	0.0019
a_6	-	-
a_7	0.0945	0.5079
a_8	-0.0015	-0.0021
a_9	-	-
a_{10}	-	-
a_{11}	-0.0051	-0.2917
a_{12}	0.0007	0.0010
a_{13}	-	-
a_{14}	-	-
a_{15}	-	-

The propeller was considered rotating in the infinite fluid mud, without a free surface. As a basic sample of fluid mud, the one having the following parameters was selected (γ_0 = 1.72, τ_s = 13.01, γ_s = 0.019, τ_f = 21.4, γ_f = 9.42, μ_∞ = 0.02, ρ = 1160). The parameter μ_∞ was varied to yield the following viscosity ratios $r_\mu = \frac{\mu_\infty}{\mu_w} \approx$ 20, 50, 100, 140, 160, where μ_w was taken to be 0.001. The stress-stain curves produced in this manner are depicted in Figure 5.

The unstructured hex-dominant grid of 5M cells was used, with the average y^+ value of 0.8. The solution of the RANS equations was done in the steady-state manner whereas the propeller rotation was modeled using the moving reference frame. This way a larger number of computations could be carried out without a considerable loss of accuracy. In Figure 6 the open water diagrams generated from the computational results are shown.

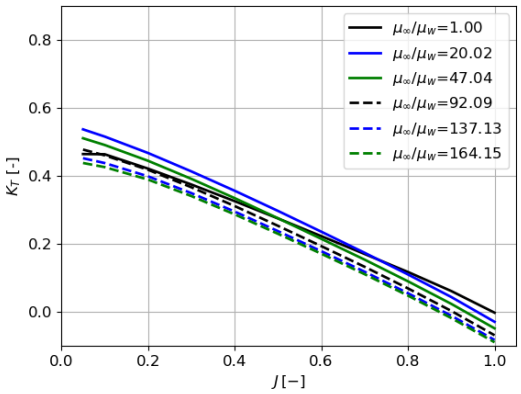

(a)

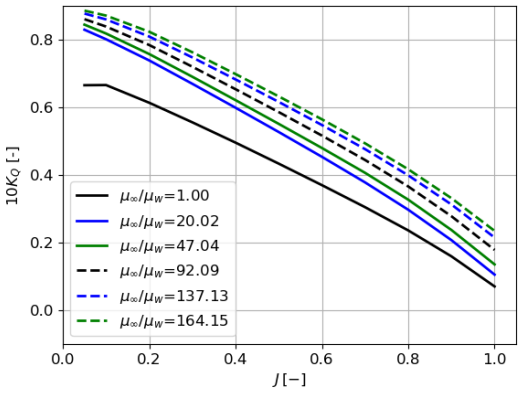

(b)

Figure 6: The open water diagram for different viscosity ratios

In order to analyze the dependence of K_T and K_Q on the viscosity ratio, the plots for the difference between the curves in the water and in the fluid mud were built , i.e. $\Delta K_T = K_T^M - K_T^W$ and $\Delta K_Q = 10\,(K_Q^M - K_Q^W)$. These are shown in Figure 7. As one can see, for $r_\mu > 20$, the curves are smooth monotonic functions and therefore can be easily fitted by polynomials. The fourth order polynomial was used which reads:

$$\begin{aligned}\Delta K_{T,Q} = a_1 + a_2 J + a_3 r_\mu + a_4 J^2 + a_5 J r_\mu + a_6 r_\mu^2 + \\ + a_7 J^3 + a_8 J^2 r_\mu + a_9 J r_\mu^2 + a_{10} r_\mu^3 + a_{11} J^4 + \\ + a_{12} J^3 r_\mu + a_{13} J^2 r_\mu^2 + a_{14} J r_\mu^3 + a_{15} r_\mu^4\end{aligned} \tag{22}$$

The fit coefficients for both K_T and K_Q are presented in

Table 5. As one can see, some of the coefficients are missing, which means that they are negligibly small ($< 10^{-4}$) and their contribution is insignificant.

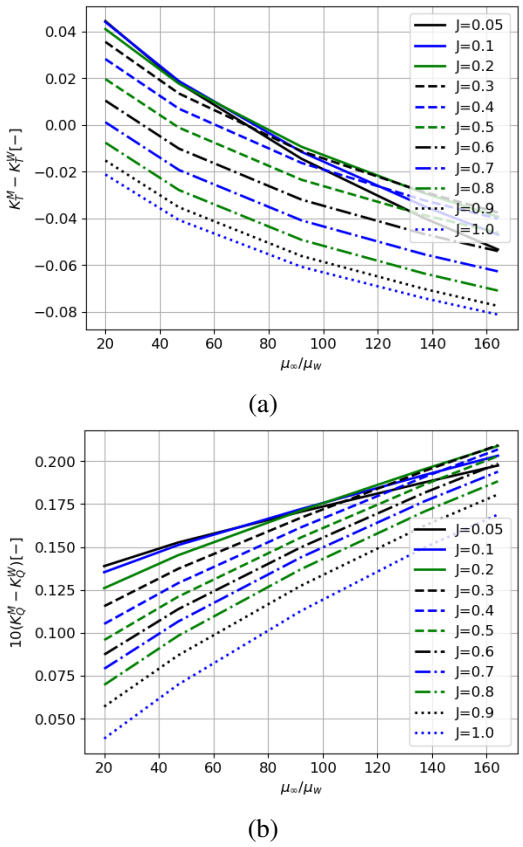

(a)

(b)

Figure 7: The difference in the open water diagram due to the change in viscosity ratio

The proposed polynomial fitting can be also represented as function of J for different r_μ, this representation is shown in Figure 8. Thus, the first part of the correlation, namely the dependence on the viscosity is ready. The tests showed, that the proposed correlations reproduce the originally generated plots from Figure 6 very well without noticeable discrepancies. Now, the dependence of the open water diagram on the degree of propeller submersion in the fluid mud has to be considered.

7 DEPENDENCE ON THE SUBMERSION DEPTH

At this step the parameters of the fluid mud itself are not changed (neither the rheological parameters, nor density), but the propeller is considered working at the interface between the fluid-mud and the water with different submersion depths, of course leading to different open-water diagrams in each case.

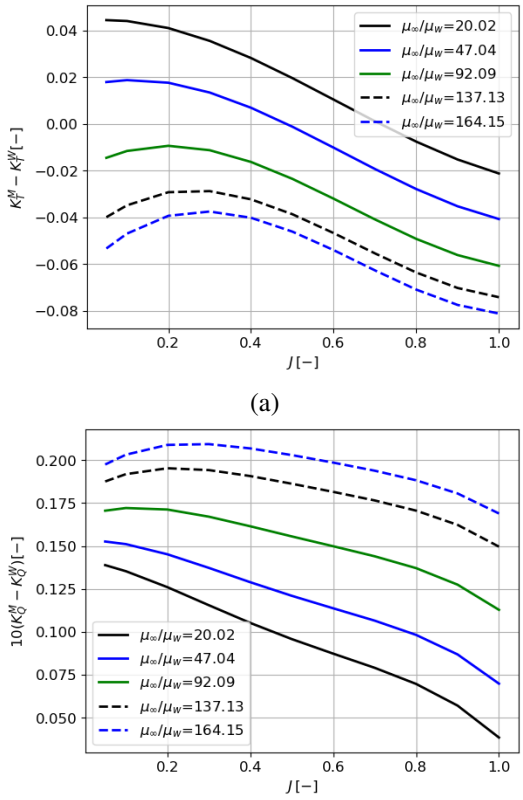

(a)

(b)

Figure 8: The difference in the open water diagram due to the change in viscosity ratio

In this package the five submersion values $s = 0$, 25, 50, 75, 100 % d, where d is the propeller diameter (see Figure 10) are considered. The values above 100% and below 0% are not taken into account. In each case the resulting open water diagram is compared to the original open water diagram without fluid mud. Therefore the correlation to be constructed also takes into account the presence of the interface as is. During the application of the proposed correlations in the actuator disk model, the parameter such as submersion in the fluid-mud is really hard to define, because in the practical situation the interface can be misaligned with the propeller axis and have a complex three-dimensional structure. Therefore, a much more reliable alternative is to use the volume fraction of fluid mud in the propeller disk instead of the distance to the fluid mud interface. Thus, for each case the submersion depth as fraction of the diameter s_p was transformed into the area fraction of fluid mud in the propeller disk $\alpha_S = \frac{S_{mud}}{S_{prop}}$ as follows:

$$\gamma = \frac{180 \arccos(1 - 8s_p(1 - s_p))}{\pi}$$

$$\alpha_S = \begin{cases} \frac{1}{2} - 2\frac{\sqrt{4s_p(1-s_p)}(\frac{1}{2}-s_p)}{\pi} - (180-\gamma)/360 \\ \text{if } 0 \le s_p \le \frac{1}{2} \\ \frac{1}{2} - 2\frac{\sqrt{4s_p(1-s_p)}(\frac{1}{2}-s_p)}{\pi} + (180-\gamma)/360 \\ \text{if } \frac{1}{2} < s_p \le 1 \end{cases},$$

where $s_p \in [0; 1]$ is $\frac{(s/d)}{100\%}$, the angles are given in degrees in this formula.

The computations were conducted using the unsteady formulation of the RANS equations. The propeller rotation was resolved, because in this case the position on the blade relative to the interface is important (as compared to the cases considered for the derivation of viscosity correlation).

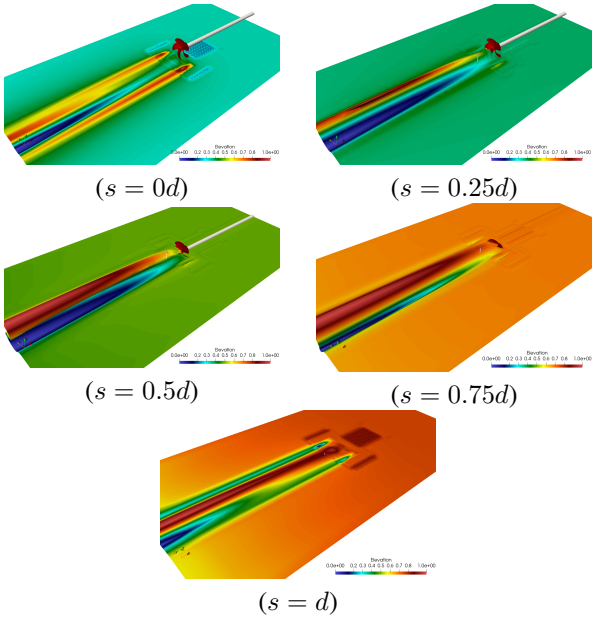

Figure 9: Distribution of the free surface elevation for different submersion depths

In order to be able to accurately resolve different interface locations, a refinement region was created for $-0.5d < z < 0.5d$, where $z = 0$ coincided with the propeller axis (for the definition of the coordinate system the reader is referred to the Figure 9). The total cell count was 6M. The parameters of the boundary layer mesh were the same as described in the previous subsection.

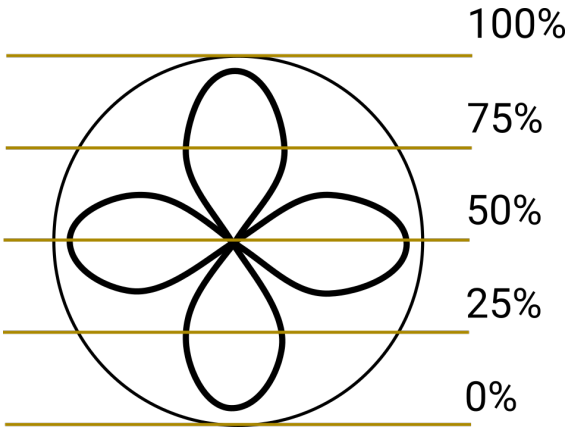

Figure 10: The scheme of different submersion depths

The total computational time was 0.5s, so 20 complete revolutions were simulated. The forces were averaged over the last 5 revolutions. In Figure 9 the resulting fluid-mud/water interface is shown. Surprisingly, the propeller rotation did not lead to intense mixing of water and fluid-mud in the propeller disk*. The deformations of the interface can be seen only downstream from the propeller and are obviously due to the generated torque. The possible explanation for this can be twofold. From the physical point of view, one can argue, that there is no actual proof that this mixing is so intense, that all fluid at the propeller is in the "average" state between water and fluid mud. From the modeling point of view the reason can be that the transport equation for the volume fraction did not include the diffusion due to turbulent mixing, which might play a significant role. Accounting for turbulent mixing would require the prior knowledge of the turbulent Schmidt number (the ratio of turbulent momentum transport to turbulent mass transport) for the water/fluid-mud which can only be obtained experimentally or using DNS.

In order to construct the correlation, first the dependence of K_T, K_Q values on α_S was analyzed for different J. These plots can be seen in Figure 11. Obviously, the K_Q always increases when α_S increase, since more of the propeller surface is covered in fluid-mud with higher viscosity, which leads to the increase of frictional resistance. On the other hand, K_T can either increase or decrease depending on J. To make the variation due to α_S more visible, the values of K_T, K_Q in water were subtracted from these curves resulting in Figure 12. Further, in order to rescale this function to always be in the range from 0 to 1, it was divided by its value for the corresponding J at $\alpha_S = 1$ (see Figure 13). This, however, can be done only if one assumes that at $\alpha_S = 1$ the open water diagram is the same as one obtained in the single phase propeller computation in infinite fluid-mud (see previous subsection). If this assumption is accepted, it becomes feasible to combine the correlations. As one can see, the curves in Figure 13 can be in the least-square sense approximated by a straight line quite accurately.

8 COMBINING THE CORRELATIONS

In order to derive the correction which would account for both effects (of r_μ and α_S) one could combine the ones from the previous sections in the following way:

$$K^M_{T,Q}(J, r_\mu, \alpha_S) = K^W_{T,Q}(J) + \alpha_S \cdot \Delta K_{T,Q}(r_\mu, J), \tag{23}$$

where $K^M_{T,Q}$ is the open water diagram in fluid-mud at particular value of r_μ and α_S, $K^W_{T,Q}$ is the open water diagram in water and $\Delta K_{T,Q}$ is the correction given by Eq. 23.

9 CONCLUSION

In the framework of this research, the numerical model of the multiphase flow containing non-Newtonian component is developed and validated for the prediction of the flat plate towed in fluid mud. Subsequently this model is used to conduct a series of computations of propeller performance in fluid mud. Based on the CFD results for different cases, the correction is derived, accounting for the influence of

*Unfortunately, there was no possibility to check in the experiment, whether this mixing would take place in reality

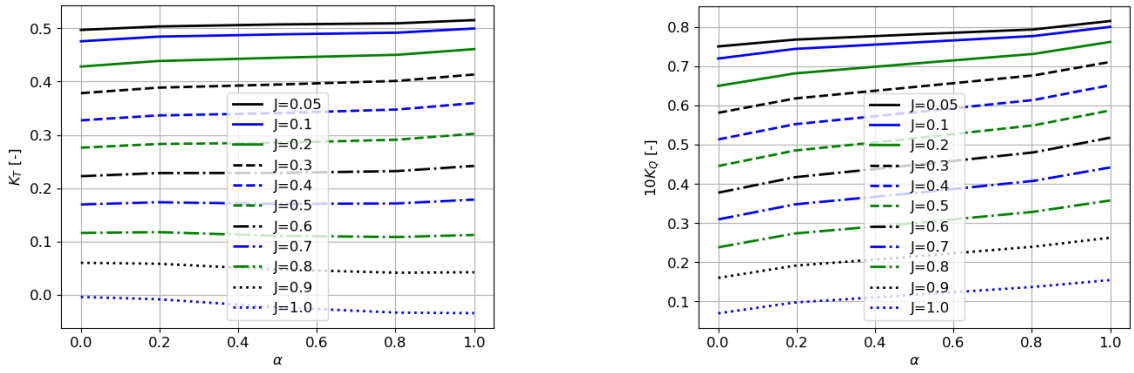

(a) (b)

Figure 11: The difference in the open water diagram due to the change of area fraction of fluid mud in the propeller disk α_s

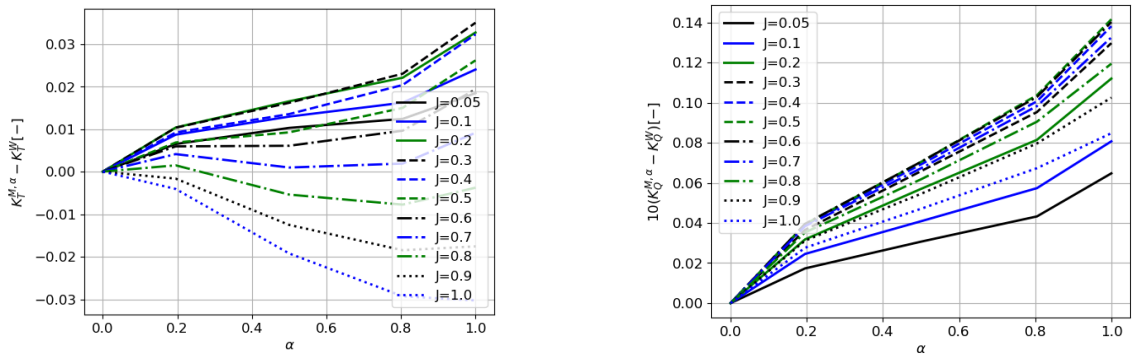

(a) (b)

Figure 12: The differences between the open water diagram in water and at some particular value of α_S: $K_T^\alpha - K_T^W$ and $10(K_Q^\alpha - K_Q^W)$

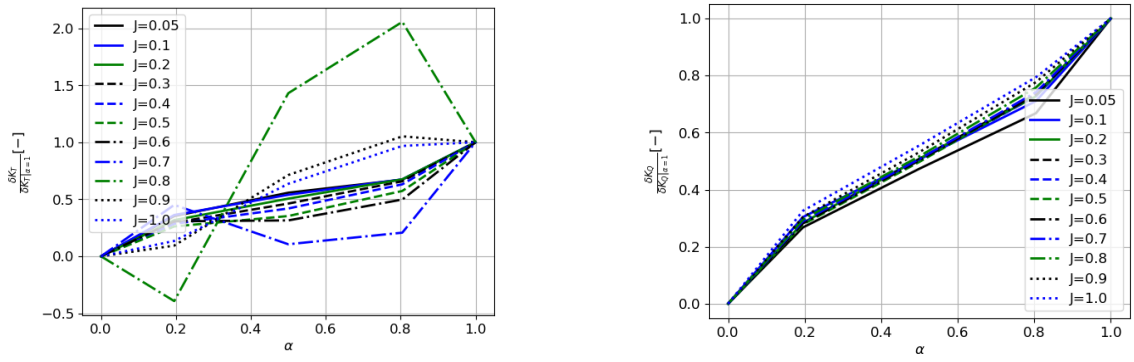

(a) (b)

Figure 13: K_T and K_Q variations divided by their values at $\alpha_S = 1$ for a particular J (i.e. $\frac{\delta K_T}{K_T^{\alpha_S=1}}$ and $\frac{\delta K_Q}{K_Q^{\alpha_S=1}}$)

parameters of the fluid mud on the propeller open-water diagram. The correction can be used in the actuator disk model during the maneuvering simulations to modify the original open-water diagram and account for the fluid-mud influence without much effort, because the values of viscosity as well as the fraction of fluid-mud in propeller plane are relatively easy to compute.

REFERENCES

El Moctar, O., Shigunov V. & Zorn, T. (2012). Duisburg test case: Post-panamax container ship for benchmarking. Ship Technology Research 59, pp. 50–64,

Gavrilov, A.A. & Rudyak, V.Y. (2016). Reynolds- averaged modeling of turbulent flows of power-law fluids. Journal of Non-Newtonian Fluid Mechanics 227, pp. 45–55.

Hanjalič, K., Popovač, M. & Hadziabdič M. (2004). A robust near-wall elliptic-relaxation eddy-viscosity turbulence model for CFD. International Journal of Heat and Fluid Flow 25(6), pp. 1047–1051.

Lovato, S., Keetels, G.H., Toxopeus, S.L. & Settels, J.W. (2022). An eddy-viscosity model for turbulent flows of Herschel–Bulkley fluids. Journal of Non-Newtonian Fluid Mechanics 301, 104729.

Lovato, S., Kirichek, A., Toxopeus, S.L., Settels, J.W. & Keetels, G.H. (2022). Validation of the resistance of a plate moving through mud: Cfd modelling and towing tank experiments. Ocean Engineering 258, 111632.

Shakeel, A. (2022). Rheological Analysis of Mud: Towards an Implementation of the Nautical Bottom Concept in the Port of Hamburg. PhD thesis, Delft University of Technology.